

A PULSAR WIND NEBULA EMBEDDED IN THE KILONOVA AT2017FGO ASSOCIATED WITH GW 170817/GRB 170817A

JIA REN¹, DA-BIN LIN¹, LU-LU ZHANG¹, XIAO-YAN LI¹, TONG LIU², RUI-JING LU¹, AND EN-WEI LIANG¹

¹Laboratory for Relativistic Astrophysics, Department of Physics, Guangxi University, Nanning 530004, China; lindabin@gxu.edu.cn

²Department of Astronomy, Xiamen University, Xiamen, Fujian 361005, China

ABSTRACT

The first detected gravitational wave GW 170817 from a binary neutron star merger is associated with an important optical transient AT2017fgo, which is a direct observation of kilonova. The recent observations suggest that the remnant compact object of the binary neutron star merger associated with GW 170817/GRB 170817A may be a stable long-lived magnetized neutron star. In this situation, there would be a pulsar wind nebula (PWN) embedded inside the dynamic ejecta. Then, we study the effect of the PWN emission on the observed light curves and radiation spectra. It is found that the characteristic emission of the embedded PWN quickly evolves. For the multi-band and long-term observations of AT2017fgo, we find that the dynamic ejecta with a PWN emission can fit the observational data very well, especially for the light curves at $t \sim 5$ days and those in the late phase. Our fitting result suggests that a PWN is embedded in the AT2017fgo.

Keywords: gravitational waves — pulsars: general — stars: neutron — gamma-ray burst: general

1. INTRODUCTION

Compact binary mergers are the main sources of gravitational wave (GW) in the frequency range of the Advanced Laser Interferometer Gravitational-wave Observatory (LIGO) and the Advanced Virgo gravitational-wave detectors. Among them, the mergers of a binary neutron star (NS) and NS-black hole (BH) draw a lot of attention since they are also the potential sources of electromagnetic radiation (EM). GW 170817 is the first GW signal from a NS-NS merger detected by the advanced LIGO and Virgo detectors on August 17 2017 12:41:04 UT (Abbott et al. 2017a). About 2 s after GW 170817, the Fermi (Goldstein et al. 2017) and INTEGRAL satellites (Savchenko et al. 2016) detected a short gamma-ray burst (GRB), GRB 170817A, from a location coincident with GW 170817. These observations were followed by a detection of an optical counterpart, AT2017fgo, associated with the accompanying macronova/kilonova powered by the radioactive decay of heavy elements formed in the NS-NS merger (Li & Paczyński 1998; Metzger & Berger 2012; Berger et al. 2013; Fernández & Metzger 2016; Ma et al. 2018; Liu et al. 2017; Song et al. 2018). The accompanying macronova/kilonova was independently confirmed by several teams (e.g., Abbott et al. 2017a; Arcavi et al. 2017; Hu et al. 2017; Lipunov et al. 2017; Smartt et al. 2017; Soares-Santos et al. 2017; Tanvir et al. 2017; Valenti et al. 2017). The observations of AT2017fgo are performed from a few hours to more than 20 days after the burst trigger until the flux is below the detection threshold. The peak frequency of the spectral energy distribution (SED) in AT2017fgo is estimated and evolves from UV band to IR band over time. In addition, the SED of AT2017fgo is found to be thermal-dominated in the early phase and evolves to a non-thermal-dominated one in the late phase (Troja et al. 2017).

The AT2017fgo is an extremely important source for understanding the physics of kilonova. The idea of kilonova was first introduced by Li & Paczyński (1998). They showed that the radioactive ejecta from a NS-NS or BH-NS merger could power a transient emission and developed a toy model to estimate the light curves. The observations reveal that the early and late phases of AT2017fgo cannot be consistently explained in the radioactivity-powered kilonova model with a single set of parameters (Cowperthwaite et al. 2017; Kasliwal et al. 2017; Kilpatrick et al. 2017; Shappee et al. 2017; Tanvir et al. 2017; Villar et al. 2017). Therefore, it was widely discussed that the merger ejecta might be consist of multi-component with different opacity, mass, velocity, and morphology. The AT2017fgo emission may be consist of an early “blue” (light r-process) component and a late “red” (heavy r-process) component (Metzger & Fernández 2014; Kasen et al. 2015, 2017). Summing the light from both a “blue” and “red” component of ejectas provides a comprehensive theoretical model of AT2017fgo (e.g., Cowperthwaite et al. 2017; Perego et al. 2017; Tanaka et al.

2017; Utsumi et al. 2017; Villar et al. 2017; Kawaguchi et al. 2018; Wanajo 2018; Waxman et al. 2018; Wu et al. 2018). However, the ejecta mass required in the multi-component model is relatively large, which is hardly met in a NS-NS merger (Yu et al. 2018). Recent works show that the remnant compact object of GW 170817 may be a stable long-lived magnetized NS. In this situation, the magnetic dipole (MD) radiation of the magnetized NS can provide an additional energy injected into the ejecta. This process would significantly increase the luminosity of the kilonova (Fan et al. 2013; Yu et al. 2013; Gao et al. 2015). With an additional energy injection from the merger central region, the ejecta mass required to explain the observations can be somewhat smaller than that in the multi-component model (Yu et al. 2018, Li et al. 2018). In fact, the ejecta with energy injection from a magnetized NS has been studied in explaining the observations of AT2017fgo (Metzger et al. 2018; Matsumoto et al. 2018; Li et al. 2018; Yu et al. 2018). However, we note that the fitting results of multi-band light curves are not quite satisfactory, especially in the late phase of light curves. This issue is presented in most of published fitting results about AT2017fgo. Another issue related to AT2017fgo is the evolution of its SED, which varied from the thermal spectrum in early phase to a non-thermal spectrum in the late phase. The above issues are our focuses in this work.

We note that the newly formed magnetized NS powers the ejecta via pulsar wind and the interaction between the pulsar wind and the ejecta leading to the formation of the following structures (see figure 2 of Kotera et al. 2013): a forward shock at the interface between the shocked and unshocked ejectas; a reverse shock at the interface between the shocked and unshocked pulsar wind (commonly called the “termination shock”). The shocked material between the forward and the reverse shocks constitutes the pulsar wind nebula (PWN, e.g. Chevalier & Fransson 1992; Gaensler & Slane 2006; Kotera et al. 2013). The PWN emission has been of interest in the field of GRB (Usov 1992; Blackman & Yi 1998; Dai & Lu 1998; Zhang & Mészáros 2001), supernovae (Vietri & Stella 1998; Inoue et al. 2003), superluminous supernovae (Thompson et al. 2004; Maeda et al. 2007; Kasen & Bildsten 2010; Murase et al. 2015; Kashiyama et al. 2016, Wang et al. 2015), and kilonovae (Gao et al. 2015; Kisaka et al. 2015; Kisaka et al. 2016). When someone with a view to a PWN-associated kilonova, it is interesting to study how the PWN radiation affects the observed light curve of kilonova, e.g., AT2017fgo.

Our article is organized as follows. In Section 2 we introduce the model we used. In Section 3 we give the model analysis and apply our model in AT2017fgo. The multi-band and long-term observations are fitted with our model. The conclusions are summarized in Section 4. Throughout this work, we use the notation $Q = 10^x Q_x$ in CGS unit unless noted otherwise.

2. DYNAMICS OF EJECTA AND PWN

Accompanying with a mass ejection of a few times $0.01M_\odot$, either a BH or NS is formed as the final remnant compact object of a NS-NS merger (e.g., Abbott et al. 2017b). The dynamic ejecta is expected to be neutron-rich and thus heavier radioactive elements are synthesized via the rapid neutron capture. The produced heavier elements are unstable and radioactively decay to heat up the ejecta, which results in ultraviolet-optical-infrared emissions. Besides, a newly formed NS deposits extra energy to power the kilonova emission via pulsar winds (Yu et al. 2013; Kasen et al. 2015; Murase et al. 2018). The interaction between the pulsar wind and the ejecta leads to the formation of a PWN between the forward and the reverse shocks (Kotera et al. 2013). The emission of PWN heats up the ejecta or leaks out of the system. Then, the observed flux is consist of the emission F_ν^b from the ejecta and the leaked part F_ν^{leak} from the PWN, i.e.,

$$F_\nu^{\text{tot}} = F_\nu^b + F_\nu^{\text{leak}}. \quad (1)$$

The estimations of F_ν^b and F_ν^{leak} are given in Sections 2.1 and 2.2, respectively.

2.1. Emission of ejecta

In this work, the dynamics and emission of the ejecta are implemented based on a simplified radiation transfer model given by Kasen & Bildsten (2010) and Metzger (2017a). The model is described as follows. The merger ejecta is divided into $N(\gg 1)$ layers with different expansion velocity v_i , where $v_1 = v_{\text{min}}$ and $v_N = v_{\text{max}}$. The location of the i th layer at time t is $R_i = v_i t$ and the mass of i th layer is $m_i = \int_{R_i}^{R_{i+1}} 4\pi r^2 \rho_{\text{ej}}(r, t) dr$ with (Nagakura et al. 2014)

$$\rho_{\text{ej}}(r, t) = \frac{(\delta - 3)M_{\text{ej}}}{4\pi R_{\text{max}}^3} \left[\left(\frac{R_{\text{min}}}{R_{\text{max}}} \right)^{3-\delta} - 1 \right]^{-1} \left(\frac{r}{R_{\text{max}}} \right)^{-\delta}, \quad (2)$$

where M_{ej} is the total mass of the ejecta and R_{max} (R_{min}) is the outermost (innermost) radius of the ejecta. The evolution of R_{max} (R_{min}) is roughly read as $R_{\text{max}} = v_{\text{max}} t$ ($R_{\text{min}} = v_{\text{min}} t$). The ejecta emission is related to the

thermal energy E_i , of which the evolution can be described as

$$\frac{dE_i}{dt} = (1 - e^{-\Delta\tau_i})e^{[-(\tau_{\text{tot}} - \tau_i)]\xi} L_{\text{md}} + m_i \dot{q}_r \eta_{\text{th}} - \frac{E_i}{R_i} \frac{dR_i}{dt} - L_i \quad \text{for } i = 1, \dots, N. \quad (3)$$

Here, the first term on the right hand side describes the energy absorbed by the i th layer for that from the central engine, the second term is the energy released via heavier radioactive elements decay in each layer, the third term is the cooling due to the adiabatic expansion, and the last term is the radiation cooling. The detail informations about parameters are presented as follows.

- The L_{md} is the power of the pulsar wind from the NS and can be estimated by MD radiation, i.e.,

$$L_{\text{md}}(t) = L_{\text{md},0} \left(1 + \frac{t}{t_{\text{sd}}}\right)^{-\alpha} \quad (4)$$

with

$$L_{\text{md},0} = \frac{B_p^2 R^6 \Omega_0^4}{6c^3} = 9.6 \times 10^{42} R_6^6 B_{p,12}^2 P_{0,-3}^{-4} \text{ erg} \cdot \text{s}^{-1}, \quad (5)$$

where Ω_0 , R , B_p , and P_0 are the initial angular frequency, radius, the surface polar magnetic field, and the initial spin period of the NS, respectively. The spin-down timescale t_{sd} and decay index α are related to the energy loss process of NS spin-down and can in principle be took as

$$t_{\text{sd}} = \frac{5c^5}{128GI\epsilon^2\Omega_0^4} = 9.1 \times 10^5 \epsilon_{-4}^{-2} I_{45}^{-1} P_{0,-3}^4 \text{ s with } \alpha = 1 \quad (6)$$

for GW-dominated spin-down loss regime and

$$t_{\text{sd}} = \frac{3c^3 I}{B_p^2 R^6 \Omega_0^2} = 2.05 \times 10^9 I_{45} B_{p,12}^{-2} P_{0,-3}^2 R_6^{-6} \text{ s with } \alpha = 2 \quad (7)$$

for MD-dominated spin-down loss regime, where G is the gravitational constant, I is the rotational inertia of NS, and ϵ is the NS ellipticity. In the first term on the right hand side of Equation (3), ξ describes the fraction of L_{md} which can be absorbed by the ejecta. In addition, τ_i is the optical depth of the i th layer for the observer and can be described as $\tau_i = \sum_{j=i}^{N-1} \Delta\tau_j$ with $\Delta\tau_j = \int_{R_j}^{R_{j+1}} \kappa\rho(r)dr$. $\tau_{\text{tot}} = \sum_{j=1}^{N-1} \Delta\tau_j = \int_{R_{\text{min}}}^{R_{\text{max}}} \kappa\rho(r)dr$ is the total optical depth of the whole ejecta in the line of sight.

- The radioactive power per unit mass \dot{q}_r and the thermalization efficiency of the radioactive power η_{th} can be read as (Korobkin et al. 2012; Barnes et al. 2016; Metzger 2017b)

$$\dot{q}_r = 4 \times 10^{18} \left[\frac{1}{2} - \frac{1}{\pi} \arctan\left(\frac{t - t_0}{\sigma}\right) \right]^{1.3} \text{ erg} \cdot \text{s}^{-1} \cdot \text{g}^{-1} \quad (8)$$

and

$$\eta_{\text{th}} = 0.36 \left[\exp(-0.56t_{\text{day}}) + \frac{\ln(1 + 0.34t_{\text{day}}^{0.74})}{0.34t_{\text{day}}^{0.74}} \right], \quad (9)$$

respectively. Here, $t_0 = 1.3$ s, $\sigma = 0.11$ s, and $t_{\text{day}} = t/1\text{day}$.

- The L_i is the radiation luminosity of the i th layer and can be estimated with

$$L_i = \frac{E_i}{\max\{t_{\text{d}}^i, t_{\text{lc}}^i\}}, \quad (10)$$

where the photon diffusion timescale t_{d}^i can be described as

$$t_{\text{d}}^i \simeq \frac{\kappa}{\beta R_i c} \sum_{j=i}^{0N-1} m_j \quad (11)$$

and the light crossing time $t_{\text{lc}}^i = R_i/c$. Here, β is a numerical factor reflecting the density distribution of the ejecta and $\beta \simeq 13.7$ is adopted in this work (Arnett 1982)¹.

¹ One can rewrite the equations (22) and (23) in Arnett (1982) as $t_{\text{d}}^i = [3\kappa/(4\pi\alpha I_M R_i c)] \sum_{j=i}^N m_j$, where the values of αI_M shown in the table 2 of Arnett (1980) are around 3 for different density distribution. Here we chose a typical value for αI_M .

The total bolometric luminosity L_{bol} of the ejecta is estimated by summing the radiation luminosity from all of layers, i.e.,

$$L_{\text{bol}} = \sum_{i=1}^{N-1} L_i. \quad (12)$$

It is always assumed that the radiation of the ejecta is from the photosphere R_{ph} with a blackbody radiation spectrum and the effective temperature T_{eff} is described as (Xiao et al. 2017; Yu et al. 2018; Li et al. 2018)

$$T_{\text{eff}} = \left(\frac{L_{\text{bol}}}{4\pi\sigma_{\text{SB}}R_{\text{ph}}^2} \right)^{1/4}, \quad (13)$$

where σ_{SB} is the Stephan-Boltzmann constant. The photosphere radius R_{ph} is estimated by setting $\tau_{\text{ph}} = \int_{R_{\text{ph}}}^{R_{\text{max}}} \rho(r) dr = 1$ if $\tau_{\text{tot}} > 1$. If $\tau_{\text{tot}} \leq 1$, we fix R_{ph} to R_{min} . The flux density at frequency ν from the ejecta is given by

$$F_{\nu}^b = \frac{2\pi h\nu^3}{c^2} \frac{1}{\exp(h\nu/kT_{\text{eff}}) - 1} \frac{R_{\text{ph}}^2}{D_L^2}, \quad (14)$$

where h is the Planck constant, k is the Boltzmann constant, and $D_L = 40$ Mpc is the luminosity distance of AT2017fgo.

2.2. Emission of the pulsar wind nebula

At the interface between the shocked and unshocked pulsar wind (“termination shock”), electrons and positrons carried in the cold pulsar wind are accelerated to ultra-relativistic energies and the magnetic fields are amplified. The accelerated leptons and the amplified magnetic fields fill the PWN out to the radius R_{PWN} . Assuming that the magnetic energy density behind the shock is a fraction ϵ_B of the total energy density, the magnetic energy density U_B^{PWN} in the PWN can be parameterized as (Tanaka & Takahara 2010, 2013; Murase et al. 2016)

$$U_B^{\text{PWN}} = \frac{B_{\text{PWN}}^2}{8\pi} = \frac{3}{4\pi} \epsilon_B R_{\text{PWN}}^{-3}(t) \int_0^t L_{\text{md}}(s) ds. \quad (15)$$

Here, $R_{\text{PWN}} \sim R_{\text{min}}$ is took since the deceleration time of the ejecta is $t_{\text{dec}} = [3M_{\text{ej}}/(4\pi n_{\text{ism}} m_p)]^{1/3}/v_{\text{ej}} \approx 86$ years with $M_{\text{ej}} \sim 10^{-2} - 10^{-1} M_{\odot}$, $v_{\text{ej}} \sim 0.1 - 0.4c$, the circum-merger particle density $n_{\text{ism}} \sim 10^{-4} - 10^{-1} \text{cm}^{-3}$, and m_p being the proton mass. Following Murase et al. (2015), a broken power-law is adopted to describe the energy distribution of leptons behind the shock front in the PWN, i.e.,

$$\frac{dn_e}{d\gamma_e} \propto \begin{cases} \gamma_e^{-q_1}, & \gamma_m \leq \gamma_e < \gamma_b, \\ \gamma_e^{-q_2}, & \gamma_b \leq \gamma_e \leq \gamma_M, \end{cases} \quad (16)$$

where $q_1 \sim 1 - 2$ ($q_2 \sim 2 - 3$) is the low (high)-energy spectral index, $\gamma_b \sim 10^4 - 10^6$ is the characteristic Lorentz factor of the accelerated leptons in the termination shock, and γ_m (γ_M) is the minimum (maximum) Lorentz factor of leptons.

For the synchrotron emission of the PWN in this work, two break frequency are relevant. The first break frequency is the characteristic synchrotron frequency corresponding to γ_b , i.e.,

$$\nu_b \approx \frac{3}{4\pi} \gamma_b^2 \frac{q_e B_{\text{PWN}}}{m_e c}, \quad (17)$$

where q_e is the charge of leptons. The second break frequency is the synchrotron cooling frequency

$$\nu_c \approx \frac{3}{4\pi} \gamma_c^2 \frac{q_e B_{\text{PWN}}}{m_e c} \quad (18)$$

with $\gamma_c = 6\pi m_e c / (\sigma_{\text{T}} B_{\text{PWN}}^2 t)$ being the cooling Lorentz factor and σ_{T} being the Thomson cross-section (Sari et al. 1998). Owing to this cooling effect, the energy distribution of leptons may be different from Equation (16). Correspondingly, the synchrotron emission can be described as follows. In the fast-cooling regime, i.e., $\nu_c < \nu_b$, the synchrotron emission flux density L_{ν} at any frequency ν can be expressed as

$$\nu L_{\nu}^{\text{PWN}} \approx \frac{\xi L_{\text{md}}}{2R_b} \begin{cases} (\nu_c/\nu_b)^{(2-q_1)/2} (\nu/\nu_c)^{(3-q_1)/2}, & \nu \leq \nu_c, \\ (\nu/\nu_b)^{(2-q_1)/2}, & \nu_c \leq \nu \leq \nu_b, \\ (\nu/\nu_b)^{(2-q_2)/2}, & \nu_b \leq \nu \leq \nu_M; \end{cases} \quad (19)$$

in the slow-cooling regime, i.e., $\nu_c > \nu_b$, the synchrotron emission flux density can be written as

$$\nu L_\nu^{\text{PWN}} \approx \frac{\xi L_{\text{md}}}{2R_b} \begin{cases} (\nu_b/\nu_c)^{(3-q_2)/2} (\nu/\nu_b)^{(3-q_1)/2}, & \nu \leq \nu_b, \\ (\nu/\nu_c)^{(3-q_2)/2}, & \nu_b \leq \nu \leq \nu_c, \\ (\nu/\nu_c)^{(2-q_2)/2}, & \nu_c \leq \nu \leq \nu_M, \end{cases} \quad (20)$$

where $R_b \sim (2 - q_1)^{-1} + (q_2 - 2)^{-1}$ and the radiation efficiency $\xi = \eta \epsilon_e$ with $\eta = \min\{1, (\nu_b/\nu_c)^{(q_2-2)/2}\}$ (Fan & Piran 2006) is adopted. Based on Equations (19) and (20), one can have $\int_0^{+\infty} L_\nu d\nu \approx \eta \epsilon_e L_{\text{md}}$. We ignore the effect of IC scattering process because it is not the main concern of this work. Assuming that the radiation spectrum does not change after photons pass through the ejecta, the observed flux from a PWN can be described as

$$F_\nu^{\text{leak}} = \frac{L_\nu e^{-\tau_{\text{tot}}}}{4\pi D_L^2}. \quad (21)$$

3. RESULTS AND DATA FITTING

3.1. General behavior of kilonova and PWN

The emission of PWN is our main focus of the present work. Then, we first study the evolution of B_{PWN} (black line), ν_b (red line), and ν_c (blue line) for a PWN. The results are shown in Figure 1, where $v_{\text{min}} = 0.1c$, $\epsilon_B = 0.01$, $L_{\text{md},0} = 10^{41} \text{ erg} \cdot \text{s}^{-1}$ (solid lines) or $10^{42} \text{ erg} \cdot \text{s}^{-1}$ (dashed lines), $t_{\text{sd}} = 10^6 \text{ s}$, $\alpha = 1$, and $\gamma_b = 10^4$ are adopted. One can find that the magnetic field strength decreases rapidly as time goes on. It is very different from that in the PWN associated with a core-collapse supernova (e.g., figure 4 of Kotera et al. 2013). Then, one would find a PWN with quickly evolving behavior in its radiation. Figure 1 shows that the characteristic synchrotron frequency ν_b quickly decreases from X-ray band ($t \sim 0.01 \text{ d}$) to ultraviolet-optical-infrared bands ($t \sim 0.1 - 10 \text{ d}$) and even to radio band for late phase. However, the cooling frequency ν_c quickly increases from radio band to optical band. Thus, the radiation efficiency of PWN may be low in the late phase. In other words, the radiation of PWN in the late phase would be in the slow cooling regime. Figure 1 also reveals that a higher energy injection from the central NS would produce a PWN with higher B_{PWN} and ν_b but lower ν_c . Then, the transition from the fast cooling regime to the slow cooling regime would be deferred for a PWN with high energy injection. Since the characteristic synchrotron frequency enters into the optical bands quickly, Equation (3) can provide a good description about the evolution of the internal energy for a ejecta ². This is different from the situation that the PWN characteristic synchrotron frequency is in the X-ray band.

In the following two paragraphs, we study the effect of PWN emission on the observed light curves and radiation spectrum. The properties of the ejecta are described with $M_{\text{ej}} = 0.03M_\odot$, $\kappa = 5 \text{ g} \cdot \text{cm}^{-2}$, $v_{\text{max}} = 0.3c$, $\delta = 2$. We typically chose $q_1 = 1.8$ and $q_2 = 2.2$ for the PWN. Figure 2 plots the observed flux in the situations with $L_{\text{md},0} = 0$ (black lines), $10^{41} \text{ erg} \cdot \text{s}^{-1}$ (red lines), $10^{42} \text{ erg} \cdot \text{s}^{-1}$ (orange lines), and $10^{43} \text{ erg} \cdot \text{s}^{-1}$ (blue lines). The upper panels show the observed light curves at K (left panel), $F606W$ (middle panel), and U bands (right panel), respectively. Here, the monochromatic AB magnitude is estimated with $M_\nu = -2.5 \log_{10}(F_\nu/3631 \text{ Jy})$. In these panels, the solid lines plot the behavior of F_ν^{tot} and the dashed lines depict the evolution of F_ν^b . Comparing the situations with $L_{\text{md},0} = 0$ and $L_{\text{md},0} \neq 0$, one can find that the ejecta emission are very different. The energy injection from the central region can elevate the observed intensity effectively. The higher value of $L_{\text{md},0}$ adopted, the higher luminosity of ejecta would be. The more important is that the effect of energy injection on the light curves is different for different observational band. The observed flux smoothly increases in the infrared K -band, but a bimodal light curve is presented in the light curves of ultraviolet U -band or optical $F606W$ -band. The bimodal light curves have also been found in Metzger (2017b). The bimodal light curves become obvious if the injection energy is significantly high. Then, one can believe that the appearance of bimodal structure in the light curves is related to the heating of ejecta by the PWN. In the early phase, the optical depth is high, the PWN emission is mainly absorbed by the inner region of the ejecta and the radiative cooling of the ejecta mainly appears in the outer part. That is to say, the energy injection in the early phase is mainly deposited in the inner layers. With the decrease of optical depth τ_{tot} (see Figure 3), the deposited energy would be released. Then, one can find a bump in the light curves at the time of $\tau_{\text{tot}} \sim 1$. This is the reason for the bimodal light curve behavior. It is interesting to point out that the deposited energy is associated with the value of $L_{\text{md},0}$. Then, the higher $L_{\text{md},0}$ adopted, the more luminosity of the bump at $\tau_{\text{tot}} \sim 1$ would be. This is consistent with

² Due to the bound-free or bound-bound absorption of the ejecta, the optical depth of X-ray photons are much higher than that of optical photons. Since ν_b falls in the X-ray bands in the very early phase, the absorption of the PWN emission is more intense than that presented in Equation (3).

the light curves shown in Figure 2.

The lower panels of Figure 2 plot the observed radiation spectrum at $t = 1$ d (left panel), 10 d (middle panel), and 100 d (right panel), respectively. As one can find from these panels, the radiation spectrum is the superposition of a thermal component and a non-thermal (power-law) component. Over time the spectral peak of the blackbody component moves toward the lower frequency and its intensity gradually decreases. The non-thermal component emerges at a certain time and becomes dominant in the late phase. These behaviors can be understood as follows. Since the optical depth τ_{tot} is significantly high in the very early phase, the emission of the PWN is mainly absorbed by the inner layers of the ejecta. In addition, the photon diffusion timescale t_d of inner layers is sufficiently large. Then, the observed radiation is mainly from the outer layers of the ejecta and the effect of the PWN emission could not be observed. Correspondingly, the radiation spectrum would be a thermal form. This is the reason for the same behavior in the very early phase ($t \lesssim 1$ d) presented in the situations with different $L_{\text{md},0}$. As time goes on, the optical depth gradually decreases and thus the effect of PWN emission begins to emerge. However, the optical depth $\tau_{\text{tot}} (\gtrsim 1)$ is still high in this phase. In addition, the deposited energy in the inner region of the ejecta is significantly large. Then, the observed flux may be also dominated by the thermal emission of the ejecta rather than the emission from the PWN. This is consistent with those shown in the lower panels of Figure 2 at $t = 10$ d. One can also find this behavior by comparing the light curves of F_{ν}^{tot} and F_{ν}^{b} in the upper panels of Figure 2. After that, the optical depth decreases to less than unity and thus the thermal energy of the ejecta is almost all released. Then, the observed radiation would be mainly from the PWN. Correspondingly, the radiation spectrum would be dominated by the non-thermal power-law component. It can be found in the radiation spectrum of Figure 2 at $t = 100$ d.

3.2. Application on AT2017fgo

In this section, we use our model to fit the multi-band observations of AT2017fgo. The observational data of AT2017fgo is taken from Villar et al. (2017), where the data from *Hubble Space Telescope (HST)*, *Swift*, and *MASTER* optical detection are not considered in our fittings. The data used in our fits can be found in Figure 4. Our fitting is performed based on the Markov Chain Monte Carlo (MCMC) method by minimizing the total chi-square χ_{tot}^2 . Since eleven light curves on different bands should be fitted simultaneously, we adopt a time averaged chi-square to calculate the total chi-square χ_{tot}^2 . The procedure is shown as follows.

We first divide the observational time into a time serial $[0, 1\text{d}), [1\text{d}, 2\text{d}), \dots, [j-1\text{d}, j\text{d}), \dots, [25\text{d}, 26\text{d}]$. For each observational band (e.g., the i th band), we calculate the number of data points $N_{i,j}$ and the sum of chi-square $\chi_{i,j}^2$ for the data in the time interval $[j-1\text{d}, j\text{d})$. Then, the total chi-square χ_{tot}^2 is estimated with

$$\chi_{\text{tot}}^2 = \sum_{i,j} \frac{\chi_{i,j}^2}{N_{i,j} \times M_i}, \quad (22)$$

where M_i represents the accumulated number of time interval with observational data points for i th band. For the upper limit data points, e.g., the last two data points of J -band, if the theoretical results are above these data points, we multiply the obtained χ_{tot}^2 by 100 as the final total chi-square. In addition, the observational data points in the high frequency bands are scarce, e.g., B -band and U -band. Then, the last two observational data points of B -band are used to constrain the model. That is to say, if the theoretical results are not located in the error bars of these two data points, the obtained χ_{tot}^2 is also multiplied by 100 as the final total chi-square. We use the `emcee` code for our MCMC fits (Foreman-Mackey et al. 2013), where $n_{\text{walkers}} \times n_{\text{steps}} = 100 \times 600$ is adopted and the 10% of the chain in the start are eliminated. In addition, $\epsilon_B = 0.01$, $\epsilon_e = 1 - \epsilon_B$, and $\gamma_b = 10^4$ are set in our fits.

The posterior probability density functions for the physical parameters of AT2017fgo from MCMC fits are presented in Figure 5. The optimal result from MCMC fits is shown in Figure 4 with solid lines and the obtained parameters at 1σ confidence level are reported in Table 1. Figure 4 reveals a very good fits of the multi-band observations from early phase to late phase. The obtained properties of the ejecta reported in Table 1, i.e., $M_{\text{ej}} = 3.52_{-0.11}^{+0.06} \times 10^{-2} M_{\odot}$, $\kappa = 1.69_{-0.09}^{+0.06} \text{ cm}^2 \cdot \text{g}^{-1}$, and v_{min} or $v_{\text{max}} \sim (0.1 - 0.34)c$, are well consistent with those found in previous works (Kilpatrick et al. 2017; Kasliwal et al. 2017; Smartt et al. 2017; Arcavi et al. 2017; Cowperthwaite et al. 2017; Villar et al. 2017). For the value of α , $\alpha = 1$ or $\alpha = 2$ are took in our MCMC fits. However, the MCMC procedure can provide a good fitting of the observational data only in the situation with $\alpha = 1$. It suggests that the spin-down energy loss of the remnant NS after GW 170817 is in the GW-dominated spin-down loss regime, which is consistent with that found in Piro et al. (2019). With the obtained $L_{\text{md},0}$ and t_{sd} , the surface magnetic field $B_p = 1.39 \times 10^{11} \xi^{-1/2} R_6^{-3} P_{0,-3}^2$ G and the ellipticity $\epsilon = 1.97 \times 10^{-4} I_{45}^{-1/2} P_{0,-3}^2$ of the remnant NS are estimated and also consistent with those found in Yu et al. (2018) and Piro et al. (2019).

In order to test our fits result, we confront our result with *HST* observations (left panel), *Swift* observations (middle panel, *UVW1*, *UVW2*, and *UVM2* bands), *MASTER* optical observations (middle panel, *W* band), and *Spitzer Space Telescope* observations (right panel) in Figure 6. The observational data of *Spitzer Space Telescope* is from Villar et al. (2018). This figure reveals that our result is well consistent with the data from *HST*, *Swift*, *MASTER*, and *Spitzer Space Telescope*, which were not used in our MCMC fits. In observations, it is found that the observed radiation spectrum of AT2017fgo gradually deviates from the thermal radiation spectrum over time (Troja et al. 2017). Then, we plot the radiation spectrum from 11.5 d to 19.5 d after trigger based on our fits result. The radiation spectra are shown in the left panel of Figure 7, where the circles and triangles are the observational data laying closest to our selected time. One can find that our fits result describes the observed radiation spectra nicely. It is interesting to point out that the spectral peak of the thermal component moves from $\sim 10^{14}$ Hz at $t = 10.5$ d to the very low frequency at $t = 19.5$ d. Moreover, the thermal component is comparable to the non-thermal component at $t \lesssim 19.5$ d. This behavior suggests that the bolometric luminosity at $t \lesssim 19.5$ d can be well described with the thermal emission from the ejecta. In the right panel of Figure 7, we compare the thermal luminosity based on our fitting result with the observed bolometric luminosity (Waxman et al. 2018). One can find that our thermal luminosity describes the observed bolometric luminosity very well.

4. SUMMARY AND CONCLUSIONS

Recent works suggest that the remnant compact object of the NS-NS merger producing GW 170817/GRB 170817A may be a long-lived magnetized NS (Piro et al. 2019; Lü et al. 2019). In this situation, a pulsar wind is generated by the central magnetized NS and the interaction between the pulsar wind and the ejecta can form a rapidly evolving PWN. The radiation of PWN heats up the ejecta or leaks out of the system and thus can affect the observed light curves. In this work, we study the effect of PWN on the observed light curves and radiation spectrum. It is found that the radiation spectrum evolves from a thermal-dominated radiation spectrum in the early phase to a non-thermal-dominated radiation spectrum at several days. This is consistent with those found in AT2017fgo. Then, we perform a MCMC fits to the multi-band observations of AT2017fgo. It is shown that our model presents a very good description about the multi-band light curves of AT2017fgo. The obtained properties of the ejecta and the magnetized NS are well consistent with other previous works.

We thank Shan-Qin Wang and Yuan-Pei Yang for helpful discussions and suggestions. This work is supported by the National Natural Science Foundation of China (grant Nos. 11773007, 11533003, 11822304, 11851304, U1731239), the Guangxi Science Foundation (grant Nos. 2018GXNSFFA281010, 2016GXNSFDA380027, 2017AD22006, 2018GXNSFDA281033), and the Innovation Team and Outstanding Scholar Program in Guangxi Colleges.

REFERENCES

- Abbott, B. P., Abbott, R., Abbott, T. D., et al. 2017, *ApJL*, 848, L13
- Abbott, B. P., Abbott, R., Abbott, T. D., et al. 2017, *ApJL*, 850, L39
- Arcavi, I., Hosseinzadeh, G., Howell, D. A., et al. 2017, *Nature*, 551, 64
- Arnett, W. D. 1980, *ApJ*, 237, 541
- Arnett, W. D. 1982, *ApJ*, 253, 785
- Barnes, J., Kasen, D., Wu, M.-R., & Martínez-Pinedo, G. 2016, *ApJ*, 829, 110
- Berger, E., Fong, W., & Chornock, R. 2013, *ApJL*, 774, L23
- Blackman, E. G., & Yi, I. 1998, *ApJL*, 498, L31
- Chevalier, R. A., & Fransson, C. 1992, *ApJ*, 395, 540
- Cowperthwaite, P. S., Berger, E., Villar, V. A., et al. 2017, *ApJL*, 848, L17
- Dai, Z. G., & Lu, T. 1998, *A&A*, 333, L87
- Evans, P. A., Cenko, S. B., Kennea, J. A., et al. 2017, *Science*, 358, 1565
- Fan, Y., & Piran, T. 2006, *MNRAS*, 369, 197
- Fan, Y.-Z., Yu, Y.-W., Xu, D., et al. 2013, *ApJL*, 779, L25
- Fernández, R., & Metzger, B. D. 2016, *Annual Review of Nuclear and Particle Science*, 66, 23
- Foreman-Mackey, D., Hogg, D. W., Lang, D., & Goodman, J. 2013, *PASP*, 125, 306
- Gaensler, B. M., & Slane, P. O. 2006, *ARA&A*, 44, 17
- Gao, H., Ding, X., Wu, X.-F., Dai, Z.-G., & Zhang, B. 2015, *ApJ*, 807, 163
- Goldstein, A., Veres, P., Burns, E., et al. 2017, *ApJL*, 848, L14
- Hu, L., Wu, X., Andreoni, I., et al. 2017, *Science Bulletin*, Vol. 62, No.21, p.1433-1438, 2017, 62, 1433
- Inoue, S., Guetta, D., & Pacini, F. 2003, *ApJ*, 583, 379
- Kasen, D., & Bildsten, L. 2010, *ApJ*, 717, 245
- Kasen, D., Fernández, R., & Metzger, B. D. 2015, *MNRAS*, 450, 1777
- Kasen, D., Metzger, B., Barnes, J., Quataert, E., & Ramirez-Ruiz, E. 2017, *Nature*, 551, 80
- Kashiyama, K., Murase, K., Bartos, I., Kiuchi, K., & Margutti, R. 2016, *ApJ*, 818, 94
- Kasliwal, M. M., Nakar, E., Singer, L. P., et al. 2017, *Science*, 358, 1559
- Kawaguchi, K., Shibata, M., & Tanaka, M. 2018, *ApJL*, 865, L21
- Kilpatrick, C. D., Foley, R. J., Kasen, D., et al. 2017, *Science*, 358, 1583
- Kisaka, S., Ioka, K., & Takami, H. 2015, *ApJ*, 802, 119
- Kisaka, S., Ioka, K., & Nakar, E. 2016, *ApJ*, 818, 104
- Korobkin, O., Rosswog, S., Arcones, A., & Winteler, C. 2012, *MNRAS*, 426, 1940
- Kotera, K., Phinney, E. S., & Olinto, A. V. 2013, *MNRAS*, 432, 3228
- Li, L.-X., & Paczyński, B. 1998, *ApJL*, 507, L59
- Li, S.-Z., Liu, L.-D., Yu, Y.-W., & Zhang, B. 2018, *ApJL*, 861, L12
- Lipunov, V. M., Gorbvskoy, E., Kornilov, V. G., et al. 2017, *ApJL*, 850, L1
- Liu, T., Gu, W.-M., & Zhang, B. 2017, *NewAR*, 79, 1
- Lü, H.-J., Shen, J., Lan, L., et al. 2019, *arXiv:1904.11133*
- Ma, S.-B., Lei, W.-H., Gao, H., et al. 2018, *ApJL*, 852, L5
- Maeda, K., Tanaka, M., Nomoto, K., et al. 2007, *ApJ*, 666, 1069
- Matsumoto, T., Ioka, K., Kisaka, S., & Nakar, E. 2018, *ApJ*, 861, 55
- Metzger, B. D., & Berger, E. 2012, *ApJ*, 746, 48
- Metzger, B. D., & Fernández, R. 2014, *MNRAS*, 441, 3444
- Metzger, B. D. 2017, *arXiv:1710.05931*
- Metzger, B. D. 2017, *Living Reviews in Relativity*, 20, 3
- Metzger, B. D., Thompson, T. A., & Quataert, E. 2018, *ApJ*, 856, 101
- Murase, K., Kashiyama, K., Kiuchi, K., & Bartos, I. 2015, *ApJ*, 805, 82
- Murase, K., Kashiyama, K., & Mészáros, P. 2016, *MNRAS*, 461, 1498
- Murase, K., Toomey, M. W., Fang, K., et al. 2018, *ApJ*, 854, 60
- Nagakura, H., Hotokezaka, K., Sekiguchi, Y., Shibata, M., & Ioka, K. 2014, *ApJL*, 784, L28
- Perego, A., Radice, D., & Bernuzzi, S. 2017, *ApJL*, 850, L37
- Piro, L., Troja, E., Zhang, B., et al. 2019, *MNRAS*, 483, 1912
- Sari, R., Piran, T., & Narayan, R. 1998, *ApJ*, 497, L17
- Savchenko, V., Ferrigno, C., Mereghetti, S., et al. 2016, *ApJL*, 820, L36
- Shappee, B. J., Simon, J. D., Drout, M. R., et al. 2017, *Science*, 358, 1574
- Smartt, S. J., Chen, T.-W., Jerkstrand, A., et al. 2017, *Nature*, 551, 75
- Soares-Santos, M., Holz, D. E., Annis, J., et al. 2017, *ApJL*, 848, L16
- Song, C.-Y., Liu, T., & Li, A. 2018, *MNRAS*, 477, 2173
- Tanaka, S. J., & Takahara, F. 2010, *ApJ*, 715, 1248
- Tanaka, S. J., & Takahara, F. 2013, *MNRAS*, 429, 2945
- Tanaka, M., Utsumi, Y., Mazzali, P. A., et al. 2017, *PASJ*, 69, 102
- Tanvir, N. R., Levan, A. J., González-Fernández, C., et al. 2017, *ApJL*, 848, L27
- Thompson, T. A., Chang, P., & Quataert, E. 2004, *ApJ*, 611, 380
- Troja, E., Piro, L., van Eerten, H., et al. 2017, *Nature*, 551, 71
- Usov, V. V. 1992, *Nature*, 357, 472
- Utsumi, Y., Tanaka, M., Tominaga, N., et al. 2017, *PASJ*, 69, 101
- Valenti, S., David, Sand, J., et al. 2017, *ApJL*, 848, L24
- Vietri, M., & Stella, L. 1998, *ApJL*, 507, L45
- Villar, V. A., Guillochon, J., Berger, E., et al. 2017, *ApJL*, 851, L21
- Villar, V. A., Cowperthwaite, P. S., Berger, E., et al. 2018, *ApJL*, 862, L11
- Wanajo, S. 2018, *ApJ*, 868, 65
- Wang, S. Q., Wang, L. J., Dai, Z. G., & Wu, X. F. 2015, *ApJ*, 799, 107
- Waxman, E., Ofek, E. O., Kushnir, D., & Gal-Yam, A. 2018, *MNRAS*, 481, 3423
- Wu, M.-R., Barnes, J., Martínez-Pinedo, G., & Metzger, B. D. 2018, *arXiv:1808.10459*
- Xiao, D., Liu, L.-D., Dai, Z.-G., & Wu, X.-F. 2017, *ApJL*, 850, L41
- Yu, Y.-W., Liu, L.-D., & Dai, Z.-G. 2018, *ApJ*, 861, 114
- Yu, Y.-W., Zhang, B., & Gao, H. 2013, *ApJL*, 776, L40
- Zhang, B., & Mészáros, P. 2001, *ApJL*, 552, L35

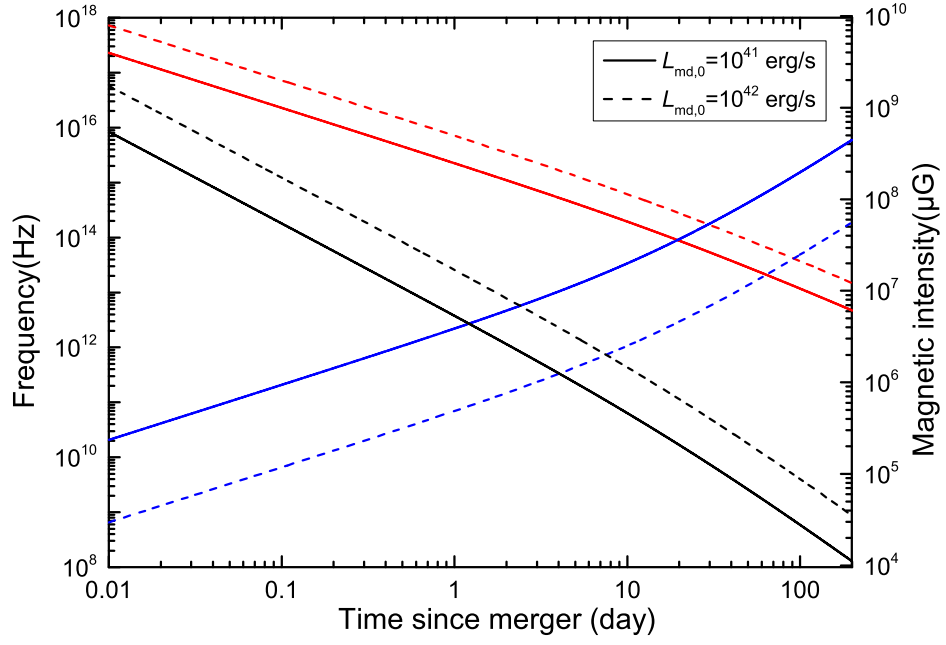


Figure 1. Evolution of B_{PWN} (black line), ν_b (red line), and ν_c (blue line) of a PWN associated with a kilonova. Here, $v_{\text{min}} = 0.1c$, $\epsilon_B = 0.01$, $L_{\text{md},0} = 10^{41} \text{ erg} \cdot \text{s}^{-1}$ (solid lines) or $10^{42} \text{ erg} \cdot \text{s}^{-1}$ (dashed lines), $t_{\text{sd}} = 10^6 \text{ s}$, $\alpha = 1$, and $\gamma_b = 10^4$ are adopted.

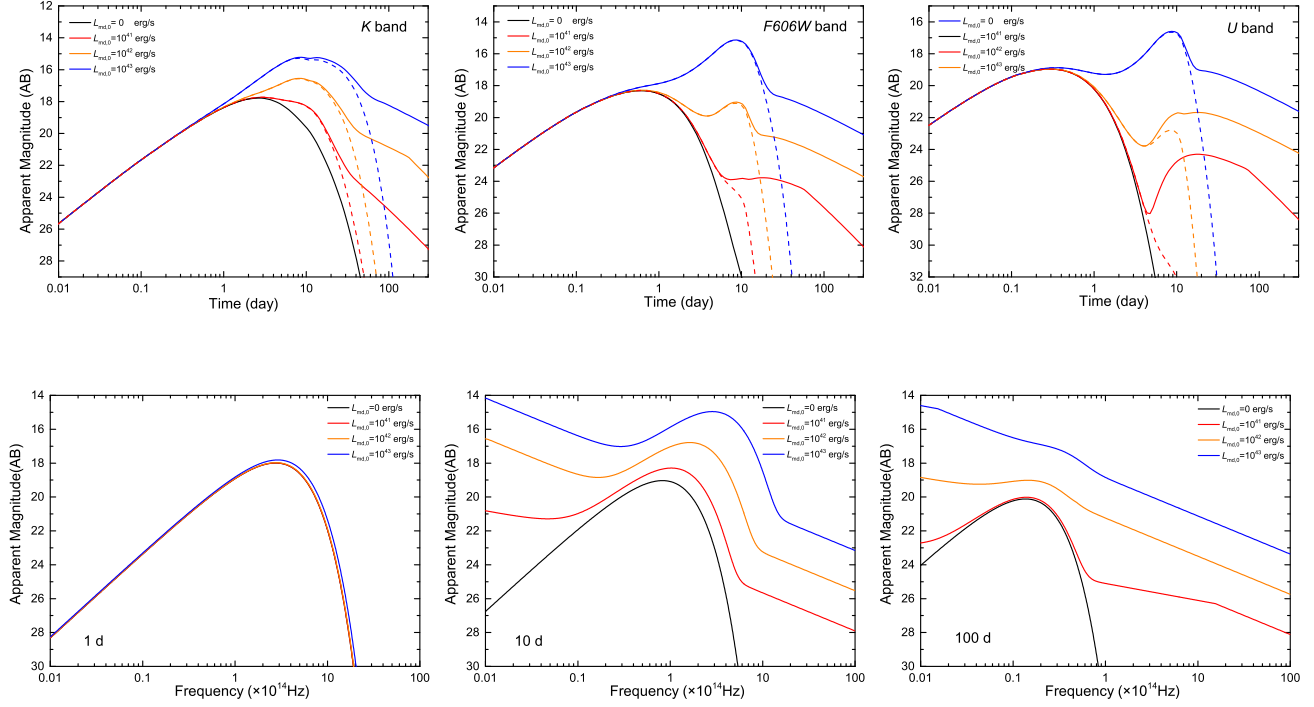


Figure 2. Light curves (upper part) and radiation spectra (bottom part) under the situations with different energy injection, i.e., $L_{\text{md},0} = 0$ (black lines), 10^{41} erg \cdot s $^{-1}$ (red lines), 10^{42} erg \cdot s $^{-1}$ (orange lines), and 10^{43} erg \cdot s $^{-1}$ (blue lines). The light curve of *K*-band, *F606W*-band, and *U*-band are shown in the left, middle, and right panels of the upper part, where the dashed lines plot the light curves of thermal emission from the ejecta. The radiation spectra at time $t = 1$ day, 10 day, and 100 day are shown in the left, middle, and right panels of the bottom part.

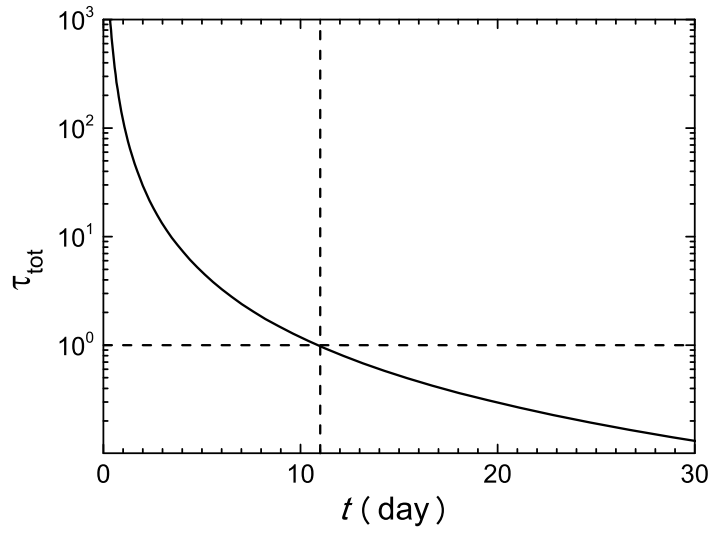


Figure 3. Evolution of τ_{tot} .

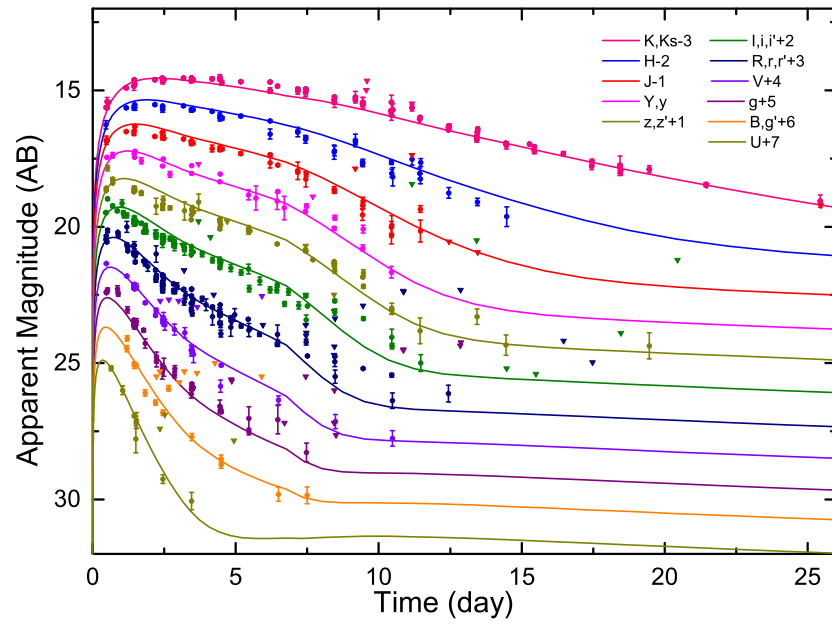


Figure 4. Fitting result (solid lines) of AT 2017gfo, where the observational data is described with circle and the upper limits are represented with triangle.

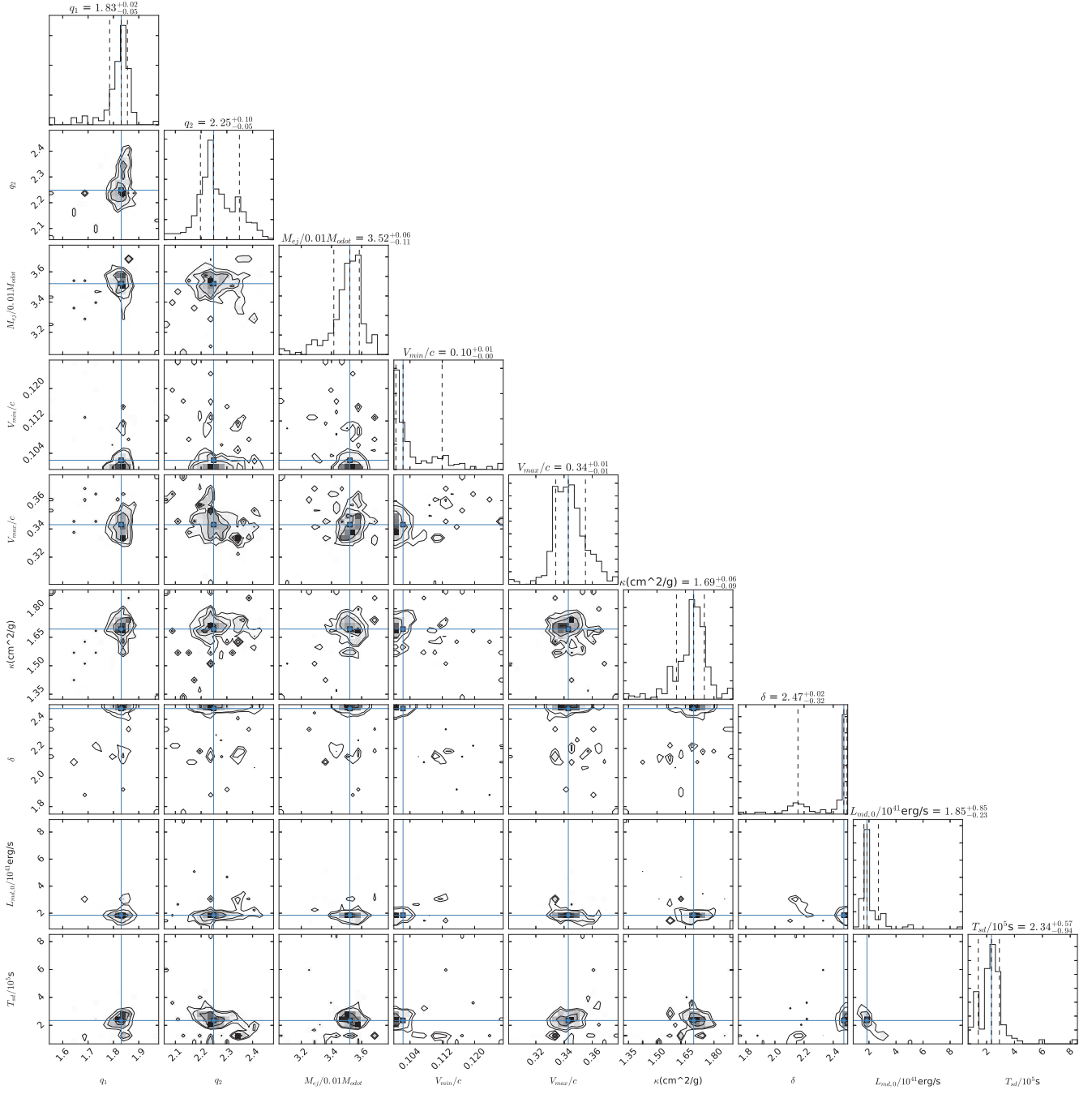


Figure 5. Posterior probability density functions for the physical parameters of AT 2017fgo from MCMC simulations.

Table 1. Fitting result from MCMC fitting.

Parameter	Constraint
$L_{\text{md},0}/10^{41}\text{erg} \cdot \text{s}^{-1}$	$1.85^{+0.85}_{-0.23}$
$t_{\text{sd}}/10^5 \text{ s}$	$2.34^{+0.57}_{-0.94}$
$M_{\text{ej}}/0.01M_{\odot}$	$3.52^{+0.06}_{-0.11}$
$\kappa/\text{g} \cdot \text{cm}^{-2}$	$1.69^{+0.06}_{-0.09}$
v_{min}/c	$0.10^{+0.01}_{-0.00}$
v_{max}/c	$0.34^{+0.01}_{-0.01}$
δ	$2.47^{+0.02}_{-0.32}$
q_1	$1.83^{+0.02}_{-0.05}$
q_2	$2.25^{+0.10}_{-0.05}$
α	1

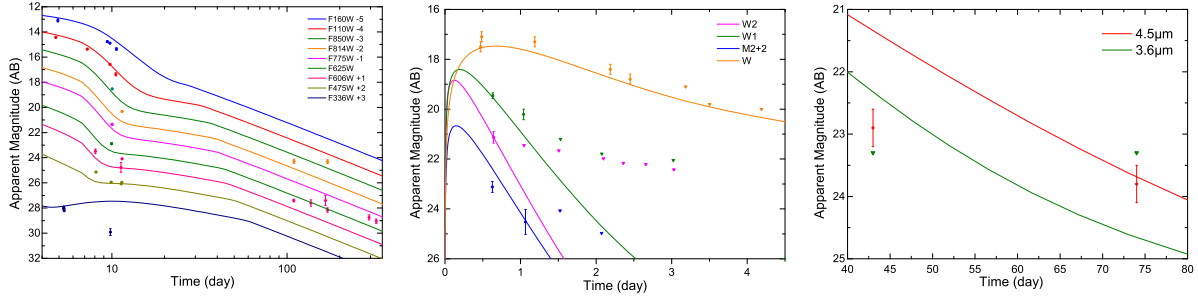


Figure 6. Confronting out fitting result with *HST* observations (left panel), *Swift* observations (middle panel, *UVW1*, *UVW2*, and *UVM2* bands), *MASTER* optical observations (middle panel, *W* band), and *Spitzer Space Telescope* observations (right panel).

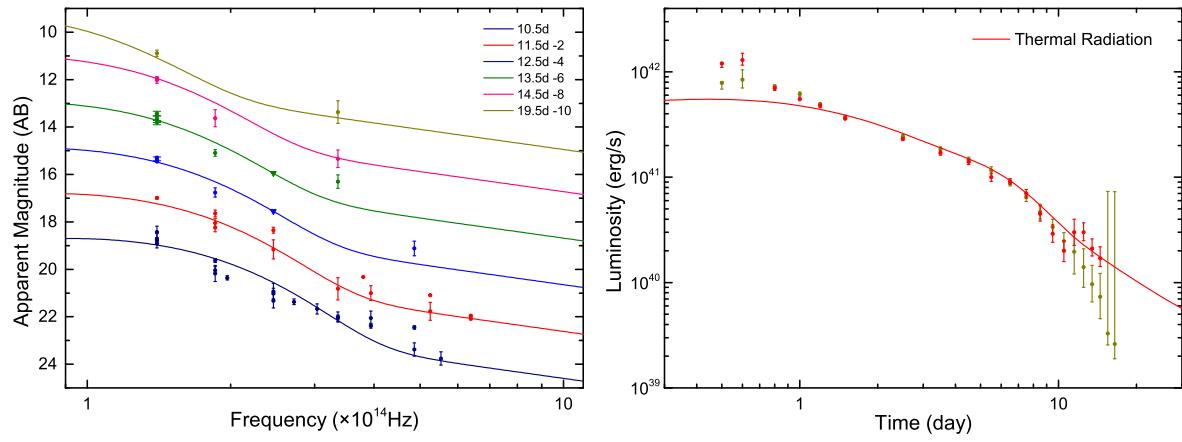


Figure 7. Comparison of radiation spectra (left panel) and bolometric luminosity (right panel).